ELSEVIER

Polymer 43 (2002) 2889–2896

polymer

www.elsevier.com/locate/polymer

Compound liquid jets at low Reynolds numbers

J.I. Ramos*

Room I-320-D, E.T.S. Ingenieros Industriales, Universidad de Málaga, Plaza El Ejido, s/n, 29013 Malaga, Spain

Received 4 January 2001; received in revised form 7 January 2002; accepted 21 January 2002

Abstract

Asymptotic methods based on the slenderness ratio are used to obtain the leading-order equations which govern the fluid dynamics of axisymmetric, isothermal, Newtonian, compound liquid jets such as those employed in the manufacture of textile fibres, composite fibres and optical fibres, at low Reynolds numbers. It is shown that the leading-order equations are one-dimensional, and analytical solutions are obtained for steady flows at zero Reynolds numbers, zero gravitational pull, and inertialess jets. A linear stability analysis of the viscous flow regime indicates that the stability of compound jets is governed by the same eigenvalue equation as that for the spinning of round fibres and annular jets. Numerical studies of the time-dependent equations subject to axial velocity perturbations at either the nozzle exit or the take-up point, or both, indicate that the compound jet dynamics evolves from periodic to chaotic motions as the extension or draw ratio is increased. The power spectrum of the inner (round) jet's radius at the take-up point broadens and the phase diagrams exhibit holes at large draw ratios. The number of holes increases as the draw ratio is increased, thus indicating chaotic behaviour. It is also shown that the nonlinear dynamics of bicomponent, compound jets is analogous to that of single-component, annular jets.

Keywords: Compound liquid jets; Low Reynolds numbers; Linear stability

1. Introduction

Most of the man-made fibres used in textile industries are manufactured by means of fibre spinning processes which consist of the steady extrusion of hot melts through a series of small holes in a plate (spinnerets) into ambient air; the resulting extrudates are simultaneously extended and wound up on a rapidly rotating drum (godet). Freezing takes place between the spinneret and the godet, and, usually, large extensions rates, rapid cooling, and high speeds are involved [1]. Fibre spinning processes are also used in the manufacture of reinforced fibres and optical fibres.

Although there has been quite a lot of research on the development of one-dimensional, mathematical models for the analysis of single-component filaments and jets under both isothermal and nonisothermal conditions at low Reynolds numbers [2,3], compound fibres such as those used in reinforced materials and optical fibres (which are manufactured in coextrusion processes) have received very little attention despite the fact that the combination of two or more different materials with different properties may result in composite fibres with highly desirable properties [4–9]. For example, in the manufacture of optical fibres, the core is surrounded by a sheath of cladding material.

Park [4] used perturbations methods based on the slenderness ratio and the smallness of the Deborah number in his studies of steady, isothermal, two-phase or compound fibres consisting of a Newtonian core layer surrounded by a sheath of non-Newtonian layer with a Maxwell rheology. His studies result in a system of ordinary differential equations for the axial velocity component and radii of the two-phase fibre, which is more manageable than the two-dimensional conservation equations of mass and linear momentum from which it was derived. Lee and Park [5] employed the one-dimensional equations developed by Schultz [10] to study the linear stability of the spinning of isothermal, bicomponent fibres characterized by a Newtonian fluid for the core and an upper-convected Maxwell fluid for the cladding, and showed that the stability of the fibre can be maintained at higher draw ratios than obtainable when the same fluid is employed for both the core and the cladding. Naboulsi and Bechtel [8] introduced a one-dimensional model of isothermal, Newtonian, bicomponent fibre filaments by integrating the three-dimensional equations over the filament cross-section, and examined the influence of density, viscosity and surface tension ratios on the steady state fluid dynamics of compound jets at low Reynolds numbers. Ji and Yang [6] and Ji et al. [7] studied isothermal, bicomponent fibres

* Tel.: +34-95-2131402; fax: +34-95-2132816.
E-mail address: jirs@lcc.uma.es (J.I. Ramos).

0032-3861/02/$ - see front matter
PII: S0032-3861(02)00086-1

characterized by a Newtonian fluid for the core and a Phan-Thien/Tanner fluid for the cladding.

Previous studies of isothermal, bicomponent or compound fibres at low Reynolds numbers [4–9] have considered isothermal, steady state flows or determined the linear stability of these flows; however, none of these studies has considered the possible steady state solutions of isothermal, steady, bicomponent fibres, and determined the effects of the upstream and downstream boundary conditions, i.e. the conditions at both the nozzle exit and the take-up point, forcing and fluid dynamics parameters on the nonlinear dynamics of compound liquid fibres.

The objective of this paper is several fold. First, the leading-order fluid dynamics equations of compound, isothermal, Newtonian jets at low Reynolds numbers are derived by means of perturbation methods based on the slenderness ratio [3,9,12]. Since the derivation of the leading-order equations is analogous to that reported in Ref. [12] for single-component annular jets, only a brief description of the steps employed in such a derivation are provided. Second, analytical solutions to the steady state solutions are obtained for several flow regimes. For the viscous flow regime, i.e. zero Reynolds number, a linear stability analysis can be performed analytically and shown to be governed by the same eigenvalue equation as that for isothermal, round jets at low Reynolds numbers [11] and single-component, annular liquid jets [12]. Third, numerical studies of the time-dependent equations are performed in order to determine the nonlinear dynamics of compound jets as a function of the nondimensional parameters that govern the flow, and the location, amplitude and frequency of the applied velocity perturbations. These studies are performed for axial velocity components at either the upstream boundary, i.e. at the nozzle exit, or the downstream boundary, i.e. at the take-up point, higher and lower than those determined from the linear stability analysis, and indicate that the nonlinear dynamics of bicomponent compound jets is similar to that of single-component, annular jets for take-up velocities greater than the critical one obtained from the linear stability analysis.

2. Formulation

Consider an axisymmetric, compound liquid jet such as the one shown schematically in Fig. 1, consisting of two immiscible, incompressible (constant density) fluids which are isothermal and Newtonian. The inner (round, subscript 1) and outer (annular, subscript 2) jets correspond to $0 \leq r \leq R(t,x)$ and $R(t,x) \leq r \leq R_2(t,x)$, respectively, where t is time, x is the axial coordinate, and R and R_2 denote the inner jet's radius and the outer jet's outer radius, respectively. The fluid dynamics of the compound jet are governed by the two-dimensional conservation equations of mass and linear momentum in the radial (r) and axial directions, appropriate boundary conditions at the nozzle exit ($x = 0$), downstream or take-up location ($x = L$), initial conditions, symmetry boundary conditions at $r = 0$, and kinematic and dynamic boundary conditions at $R(t,x)$ and $R_2(t,x)$. These equations and kinematic and dynamic boundary conditions (except for those at the symmetry axis) are analogous to Eqs. (1)–(3) and Eqs. (4), (5), (7) and (8) of Ref. [12] for $r = R_2(t,x)$, whereas those at $r = R(t,x)$ are concerned with the continuity of the tangential stresses and the jump of normal stresses due to surface tension. Since the equations and interfacial boundary conditions for compound jets are analogous to those of Ref. [12] except for those at $r = 0$ and $r = R(t,x)$, they are not presented here. However, it is emphasized that, in this paper, there is a Newtonian jet in $0 \leq r \leq R(t,x)$, whereas a passive gas occupied this region when dealing with annular liquid jets [12]. In addition, the problem considered in this paper includes two different materials characterized by their densities ρ_i and dynamic viscosities μ_i, $i = 1,2$, and two surface tensions, σ_i, $i = 1,2$ at $r = R$ and $r = R_2$, respectively.

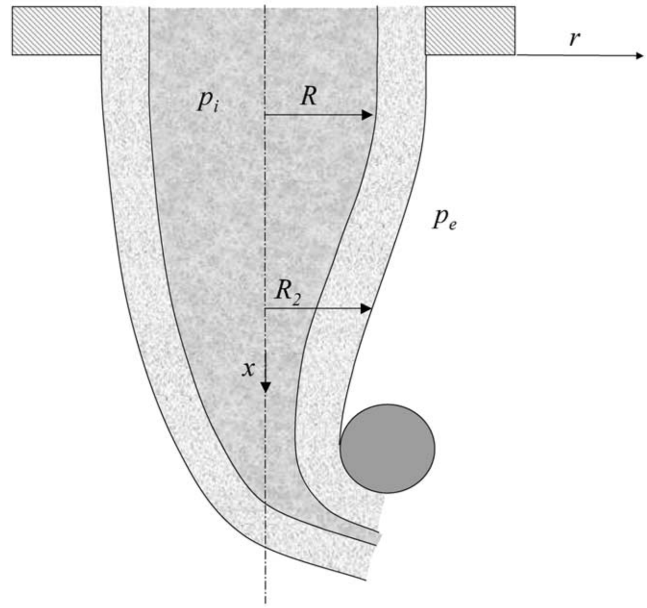

Fig. 1. Schematic of a compound liquid jet.

For slender compound jets at low Reynolds number, i.e. $\epsilon = R_0/\lambda \ll 1$, it is convenient to nondimensionalize r, x, t, u, v and p with respect to R_0, λ, λ/u_0, u_0, v_0 and $\mu u_0/\lambda$, respectively, where R_0 and λ denote a characteristic radius and a characteristic wave length in the axial direction, respectively, u_0 is a characteristic (constant) axial velocity component, $v_0 = R_0 u_0/\lambda$, v is the radial velocity component, p is the pressure, and μ is a reference viscosity. Here, we will take the reference viscosity as μ_2. Using this nondimensionalization, one can easily deduce that the resulting nondimensional equations and boundary conditions depend on ϵ, and the Reynolds, Froude and capillary numbers, i.e.

$$Re_2 = \frac{\rho_2 u_0 R_0}{\mu_2}, \qquad Fr = \frac{u_0^2}{g R_0}, \qquad Ca_2 = \frac{\mu_2 u_0}{\sigma_2}, \tag{1}$$

respectively, where g is the gravitational acceleration.

For small Reynolds numbers, $Re_2 = \epsilon Re$ with $Re = O(1)$, $Fr = F/\epsilon$ and $Ca_2 = Ca/\epsilon$ and where $F = O(1)$ and $Ca = O(1)$, which correspond to large gravitational fields and large surface tension, the dependent variables R, R_2, u_i, v_i and p_i where $i = 1, 2$, can be expanded as in Ref. [12] to yield after lengthy algebra the following leading-order equations

$$Re\left(A_2 + \frac{\rho_1}{\rho_2}A_1\right)\left(\frac{\partial B}{\partial t} + B\frac{\partial B}{\partial x}\right) = \frac{Re}{F}\left(A_2 + \frac{\rho_1}{\rho_2}A_1\right) + \frac{\partial}{\partial x}\left(3\left(A_2 + \frac{\mu_1}{\mu_2}A_1\right)\frac{\partial B}{\partial x}\right) + \frac{1}{2Ca}\left(\frac{\partial R_{20}}{\partial x} + \frac{\sigma_1}{\sigma_2}\frac{\partial R_0}{\partial x}\right), \tag{2}$$

$$\frac{\partial A_2}{\partial t} + \frac{\partial (A_2 B)}{\partial x} = 0, \tag{3}$$

$$\frac{\partial A_1}{\partial t} + \frac{\partial (A_1 B)}{\partial x} = 0, \tag{4}$$

where

$$A_1 = \frac{R_0^2}{2}, \qquad A_2 = \frac{R_{20}^2 - R_0^2}{2}. \tag{5}$$

B, R_0 and R_{20} are the leading-order axial velocity component, inner jet's radius and outer jet's outer radius, and the subscripts 1 and 2 denote the inner and outer jets, respectively.

The leading-order nondimensional axial stresses on the inner and outer jets (nondimensionalized with respect to $\epsilon\pi\mu_2 u_0 R_0$) are

$$F_x^{(1)} = A_1\left(3\frac{\mu_1}{\mu_2}\frac{\partial B}{\partial x} - p_e + \frac{1}{Ca}\left(\frac{1}{R_{20}} + \frac{\sigma_1}{\sigma_2}\frac{1}{R_0}\right)\right), \tag{6}$$

$$F_x^{(2)} = A_2\left(3\frac{\partial B_2}{\partial x} - p_e - \frac{1}{CaR_{20}}\right), \tag{7}$$

respectively.

Eqs. (2)–(4) are analogous to but simpler than Eqs. (31) and (36) of Ref. [12] for annular liquid jets consisting of only a Newtonian liquid; however, the dynamics of compound jets depends on many more physical parameters such as ρ_1/ρ_2, μ_1/μ_2, and σ_1/σ_2.

3. Analytical solutions for steady jets

For steady flows, Eqs. (3) and (4) have the following solutions

$$A_1 B = Q_1, \qquad A_2 B = Q_2, \tag{8}$$

where Q_i, $i = 1, 2$, are constants, $Q_1 + Q_2 = Q_T$.

Viscous regime. For the viscous flow regime characterized by $Re = 0$ and finite values of F, and no surface tension, the leading-order axial velocity component (cf. Eq. (2)) is governed by Eq. (44) of Ref. [12], i.e.

$$B_{ss}(x) = \exp(\alpha x), \qquad A_{1_{ss}}(x) = Q_1 \exp(-\alpha x), \qquad A_{2_{ss}}(x) = Q_2 \exp(-\alpha x), \tag{9}$$

where $\alpha = \ln B(1)$, and the linear stability analysis of this regime can be performed analytically and results in the same eigenvalue problem as that for round jets [11] and annular liquid jets [12], i.e. the eigenvalue whose real part is zero corresponds to $\alpha_c = 3.00650$ and $B(1) = 20.21$; the imaginary part of this eigenvalue is $\sigma_i = 14.011$. Moreover, the linear stability analysis indicates that the eigenvalues only depend on α, i.e. the axial velocity at the take-up point, and the results obtained by Schultz and Davis [11] for round jets at low Reynolds numbers apply to compound jets. This is not surprising, for, in the viscous regime, gravitational and inertia effects (which depend on the density ratio) are absent, and Eqs. (3) and (4) can be added to obtain an equation for R_{20}.

Viscous-capillary regime. This regime is characterized by Eq. (8), and $Re = 0$ and $Re/F = 0$, i.e. Eq. (2) becomes

$$\frac{d}{dx}\left(3\left(A_2 + \frac{\mu_1}{\mu_2}A_1\right)\frac{dB}{dx}\right) + \frac{1}{2Ca}\left(\frac{dR_{20}}{dx} + \frac{\sigma_1}{\sigma_2}\frac{dR_0}{dx}\right) = 0, \tag{10}$$

and has the following solution

$$B_1 = \left(\delta \exp\left(\frac{\alpha}{2P}x\right) + \frac{Q}{\alpha}\right)^2, \tag{11}$$

where α and δ are integration constants,

$$P = 3\left(Q_2 + \frac{\mu_1}{\mu_2}Q_1\right), \qquad Q = \frac{1}{2^{1/2}Ca}\left(Q_T^{1/2} + Q_1^{1/2}\frac{\sigma}{\sigma_2}\right).$$

Note that δ and α depend on the axial velocity component at the take-up point, i.e. they depend on $B(1)$. The values of R_0 and R_{20} can be easily determined from Eqs. (3) and (4), but they are not shown here.

Viscous-gravitationless regime. This regime corresponds to Eq. (8), $F = \infty$ and $Re \neq 0$, i.e. Eq. (2) becomes

$$Re\left(A_2 + \frac{\rho_1}{\rho_2}A_1\right)B\frac{dB}{dx} = \frac{d}{dx}\left(3\left(A_2 + \frac{\mu_1}{\mu_2}A_1\right)\frac{dB}{dx}\right), \tag{12}$$

which has the following solution

$$B(x) = \frac{\alpha\beta}{P}\frac{\exp(\alpha x)}{1 - \beta\exp(\alpha x)}, \tag{13}$$

where α and $\beta = P/(\alpha + P)$ are integration constants which can be easily determined from the conditions $B(0) = 1$ and $B(1)$, and

$$P = Re\frac{Q_2 + \frac{\rho_1}{\rho_2}Q_1}{3\left(Q_2 + \frac{\mu_1}{\mu_2}Q_1\right)}. \tag{14}$$

Viscous-gravitationless-capillary regime. This regime corresponds to Eq. (8), and $Re \neq 0$ and $Re/F = 0$, i.e.

Eq. (2) becomes

$$Re\left(A_2 + \frac{\rho_1}{\rho_2}A_1\right)B\frac{dB}{dx} = \frac{d}{dx}\left(3\left(A_2 + \frac{\mu_1}{\mu_2}A_1\frac{dB}{dx}\right)\right) + \frac{1}{2Ca}\left(\frac{dR_{20}}{dx} + \frac{\sigma_1}{\sigma_2}\frac{dR_0}{dx}\right), \quad (15)$$

which can be easily integrated upon making the change $B = z^2$ and has different solutions depending on the roots of $Pz^3 + \alpha z - Q = 0$ where P and Q have been defined previously, and α is an integration constant.

Let us define $q = \alpha/3P$ and $r = Q/2P$. Then, the solution to Eq. (15) is

$$\prod_{i=1}^{3}(z - z_i)^{\prod_{j=1,j\neq i}^{3}(z_i - z_j)^{-1}} = \beta\exp\left(\frac{P}{2}x\right), \quad (16)$$

if $q^3 + r^2 < 0$ and z_i are the different (real) roots (z^*) of

$$Pz^3 + \alpha z - Q = 0. \quad (17)$$

If $q^3 + r^2 = 0$ and Eq. (17) has three identical (real) roots, the solution of Eq. (15) is

$$-\frac{1}{2}\frac{1}{(z - z^*)^2} = \beta + \frac{P}{2}x. \quad (18)$$

If $q^3 + r^2 = 0$ and Eq. (17) has two identical (real) roots z_1, the solution of Eq. (15) is

$$\left(\frac{z - z_1}{z - z_2}\right)^{1/(z_2 - z_1)^2}\exp\left(\frac{(z_2 - z_1)}{(z - z_1)}\right) = \beta\exp\left(\frac{P}{2}(z_2 - z_1)^2 x\right). \quad (19)$$

If $q^3 + r^2 > 0$ and Eq. (17) has a real root (z_1) and two complex conjugate ones ($z_r \pm iz_i$), $i^2 = -1$, the solution of Eq. (15) is

$$\beta + \frac{P}{2}x = -\frac{1}{(z_1 - z_r)^2 + z_i^2} \times \left(\frac{z_1 - z_r}{z_i}\arctan\frac{z - z_r}{z_i} + \ln\frac{\left((z - z_r)^2 + z_i^2\right)^{1/2}}{z - z_1}\right). \quad (20)$$

In Eqs. (16)–(20), β and α are integration constants which can be determined from the condition $B(0) = 1$ and depend on the value of the take-up velocity, i.e. $B(1)$.

The linear stability of the viscous-gravitationless, viscous-capillary and viscous-gravitationless-capillary regimes whose steady state solutions have been obtained in the previous paragraphs requires the use of numerical techniques based upon the discretization of the equations for the perturbed quantities.

4. Presentation of results

As shown in previous sections, the nonlinear dynamics of steady, isothermal, Newtonian, compound liquid jets at low Reynolds numbers depends on Re, Re/F, Ca, p_e, ρ_1/ρ_2, μ_1/μ_2, σ_1/σ_2, Q_1, Q_2 and $B_{ss}(1)$.

Some sample results illustrating the steady state compound jet's geometry and axial velocity component are presented in Figs. 2 and 3. These figures were obtained by solving numerically the steady state equations presented in previous sections by means of a second-order accurate finite difference method; the number of grid points was at least 2001, $B(0) = 1$ and $R(0) = 1$. Fig. 2 indicates that the axial velocity increases rapidly near the downstream or take-up point. The axial traction on the inner round jet also increases quite rapidly near the take-up point, except at low Reynolds numbers for which it increases rather smoothly from the upstream to the downstream boundaries. The compound jet's geometry shown in Fig. 2 clearly shows the jet's contraction near the nozzle exit at low Reynolds numbers; the contraction at higher Reynolds numbers is large at the take-up point where the axial velocity component is largest. Fig. 2 also indicates that the ratio of the axial traction on the inner jet to that on the outer one (hereon, referred to as the axial traction ratio) is largest at the upstream boundary and increases as the Reynolds number is increased; this ratio decreases downstream and tends towards a value equal to unity.

The steady state compound jet's radii were found to increase slightly as Re/F was decreased due to the gravitational pull; the axial velocity component and axial traction on the inner jet increase slightly as Re/F was increased for the values of the parameters shown in Fig. 2 and $Re/F = 1$, 10 and 0.1. The ratio of traction forces at the nozzle exit or die was found to be about 1.16, 1.15 and 1.12 for $Re/F = 0.1$, 1 and 10, respectively, and decreased towards unity at the downstream boundary.

The compound jet's geometry, leading-order axial velocity and axial traction force on the inner jet were not found to be very sensitive to the capillary number for $Ca = 1$, 10 and 0.5; however, the ratio of axial traction forces at the upstream boundary was found to be equal to about 1.45, 1.15 and 1.02 for $Ca = 0.5$, 1 and 10, respectively.

The steady state compound jet's radii and the thickness of the steep region at the downstream boundary were found to increase as ρ_1/ρ_2 was increased as indicated in Fig. 3; both the axial traction force on the inner jet and its gradient increase at the downstream boundary as ρ_1/ρ_2 was increased. The ratio of axial traction forces at the upstream boundary was found to be equal to about 1.75, 1.15 and 1.12 for $\rho_1/\rho_2 = 5$, 1 and 0.5, respectively.

The steady state compound jet's radii and the thickness of the steep region at the downstream boundary were found to increase as μ_1/μ_2 was decreased; the axial traction force on the inner jet increases whereas its gradient at the downstream boundary decreases as μ_1/μ_2 is increased. The ratio of axial traction forces at the upstream boundary was found to be equal to about 3.75, 1.15 and 0.20 for $\mu_1/\mu_2 = 0.5$, 1 and 10, respectively.

The compound jet's geometry, leading-order axial

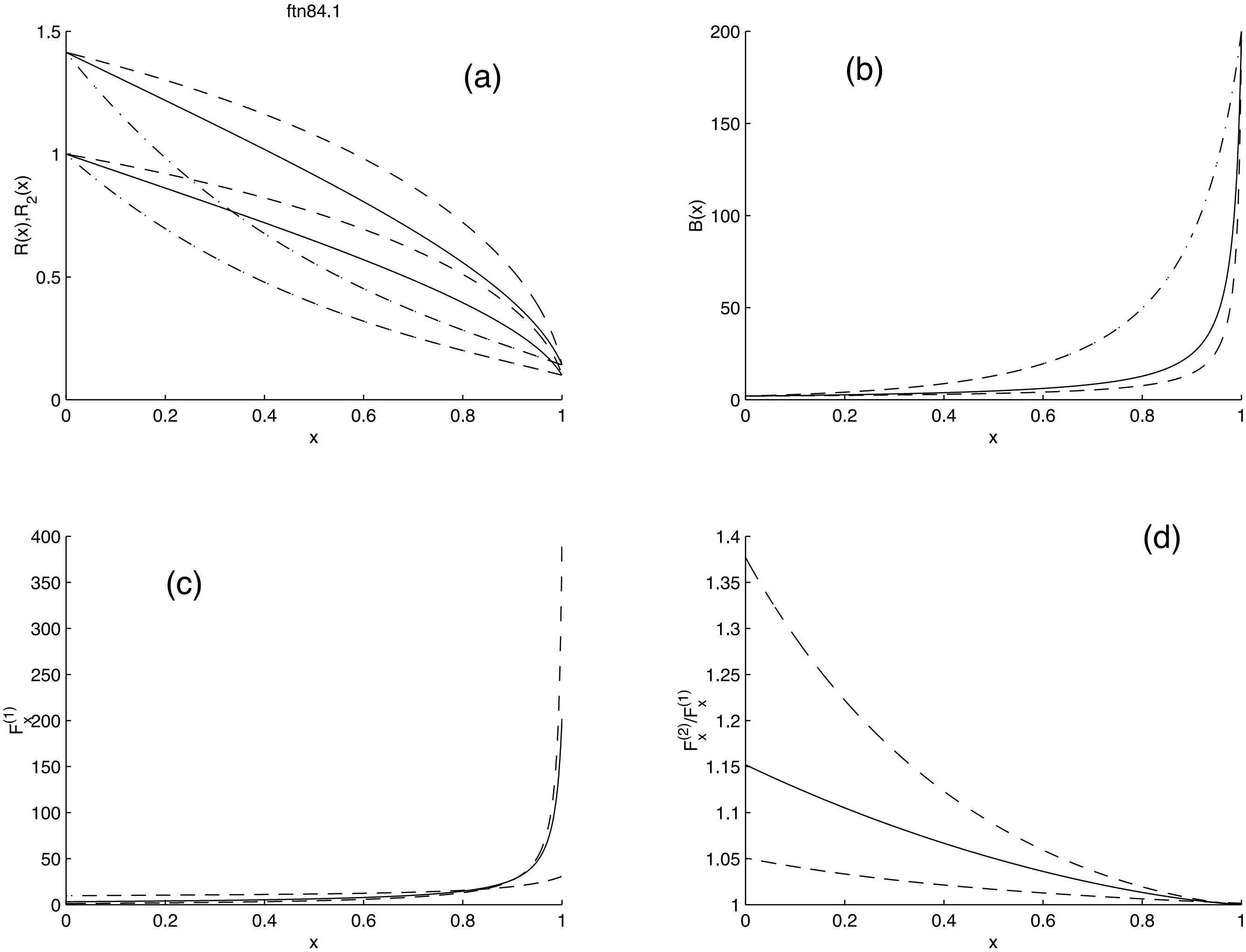

Fig. 2. (a) Compound jet's geometry, (b) axial velocity component, (c) axial traction on the inner jet and (d) ratio of axial traction on the outer jet to that on the inner one. ($Re/Fr = 1$, $Ca = 1$, $\rho_1/\rho_2 = 1$, $\mu_1/\mu_2 = 1$, $\sigma_1/\sigma_2 = 1$, $p_e = 0$, $Q_1 = 1$, $Q_2 = 1$, $R(0) = 1$, $B(0) = 1$, $B_{ss}(1) = 100$. Solid lines: $Re = 1$; dashed lines: $Re = 2$; dashed-dotted lines: $Re = 0.1$).

velocity and axial traction force on the inner jet were not found to be very sensitive to σ_1/σ_2 and p_e; however, the ratio of axial traction forces at the upstream boundary was found to be equal to about 1.15, 1.07 and 1.01 for $\sigma_1/\sigma_2 = 1$, 0.5 and 0.1, respectively, and equal to about 1.18 and 1.15 for $p_e = 1$ and 0, respectively.

For $R(0) = 1$, it has been observed that an increase in Q_1 results in an increase in $B(0)$, a decrease in $R_2(0)$, and a large contraction of the compound jet near the take-up point. Both $B(1)$ and the axial traction force on the inner jet at the take-up point increase as Q_1 is increased, while the ratio of axial traction forces at the nozzle exit is about 21 for $Q_1 = 0.1$. An increase in Q_2 with $B(0) = 1$ results in an increase in $R_2(x)$; however, the axial velocity component and the axial traction force are not very sensitive to Q_2. The ratio of axial traction forces at the upstream boundary was found to be equal to about 2.23 and 0.20 for $Q_2 = 2$ and 0.1, respectively.

The nonlinear dynamics of compound jets subject to time-dependent perturbations was studied by solving numerically Eqs. (2)–(4) for take-up speeds smaller than, equal to or larger than the critical one obtained from the linear stability analysis of the viscous flow regime. It must be noted that the time-dependent dynamics of compound jets depends on the nondimensional parameters mentioned above and the amplitude and forcing of the imposed perturbations. For axial velocity perturbations at either the nozzle exit or the take-up point, the leading-order axial velocity employed in the time-dependent studies is

$$B(t, x_j) = B_{ss}(x_j)(1 + a_j \sin S_j t), \tag{21}$$

where a_j and S_j denote the (nondimensional) amplitude and frequency of the imposed forcing at x_j, and $(j, x_j) = (i, 0)$ and $(e, 1)$ denote the nozzle exit and the take-up point, respectively.

The numerical results corresponding to $Re = 10^{-4}$, $Re/F = 0$, $Ca = 10^{39}$, $\rho_1/\rho_2 = 1$, $\mu_1/\mu_2 = 1$, $\sigma_1/\sigma_2 = 1$, $p_e = 0$, $Q_1 = 0.50$, $Q_2 = 1 - Q_1$, $B_{ss}(0) = 1$, $\mathrm{Rad} = 0.20$,

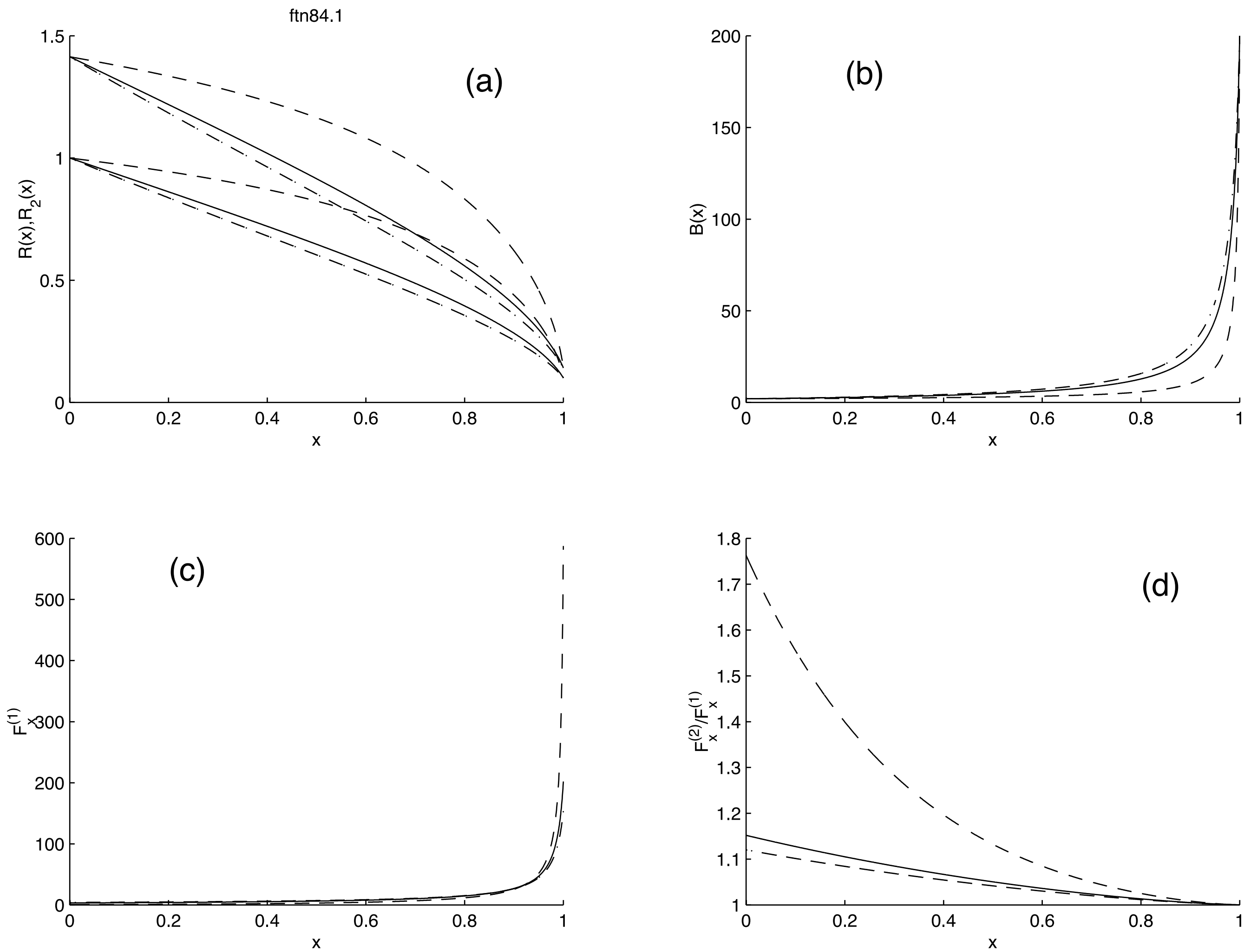

Fig. 3. (a) Compound jet's geometry, (b) axial velocity component, (c) axial traction on the inner jet and (d) ratio of axial traction on the outer jet to that on the inner one. ($Re = 1$, $Re/Fr = 1$, $Ca = 1$, $\mu_1/\mu_2 = 1$, $\sigma_1/\sigma_2 = 1$, $p_e = 0$, $Q_1 = 1$, $Q_2 = 1$, $R(0) = 1$, $B(0) = 1$, $B_{ss}(1) = 100$. Solid lines: $\rho_1/\rho_2 = 1$; dashed lines: $\rho_1/\rho_2 = 5$; dashed-dotted lines: $\rho_1/\rho_2 = 0.5$).

$B_{ss}(1) = 2Q_1/\mathrm{Rad}^2$, $a_i = 0.05$, $a_e = 0$, $S_i = 1$, $S_e = 1$ indicate that the compound jet's radii and axial traction forces on the inner and outer jets at the take-up point are periodic functions of time which have the same frequency as that of the imposed axial velocity perturbation at the nozzle exit or die, i.e. at $x = 0$. The amplitude of the compound jet's radius at the interface between the inner and outer jets is about 0.002 which is much smaller than the mean value of the inner jet's outer radius. This periodic behaviour is also observed in both the power spectrum and phase diagram of $R(t, 1)$; the power spectrum is characterized by a single peak at a frequency equal to that of the imposed velocity perturbations, i.e. $1/2\pi$, and the phase diagram is a circumference.

The numerical results corresponding to the above set of parameters except that $B_{ss}(1) \approx 44.5 > B_c$ indicate that the compound jet's radii and axial traction force on the inner jet at the take-up point are spiky, and their maximum values seem to be modulated with a frequency of the order of that the imposed velocity perturbations, whereas the ratio of axial traction forces is constant. Moreover, the power spectrum of $R(t, 1)$ is characterized by several peaks, and the frequency associated with these peaks is not related to that of the applied velocity perturbations. In addition, the phase diagram for $R(t, 1)$ has a duck's beak shape, presents corrugations on its periphery, is thick, and contains some holes, i.e. regions which are never visited. This phase diagram is analogous to that presented in Fig. 7 of Ref. [12] for annular jets, and the largest and smallest values of $R(t, 1)$ are larger and smaller, respectively, and the values of $(\mathrm{d}R/\mathrm{d}t)(t, 1)$ are larger than those corresponding to $B_{ss}(1) \approx 25$.

For the same set of parameters as above except that $B_{ss}(1) = 100$, the numerical results indicate that the leading-order axial velocity component, jet's radii and axial traction forces are spiky functions of time, where the largest and smallest values of $R(t, 1)$ increase and decrease, respectively, as $B_{ss}(1)$ is increased; the axial traction force also increases as $B_{ss}(1)$ is increased in accord with the large gradient of the axial velocity at the take-up point. Moreover, the amplitude of the modulation of the spikes in the compound jet's radii and axial traction force on the inner jet at the take-up point for $B_{ss}(1) = 100$ are smaller than for $B_{ss}(1) \approx 44.5$. This is also observed in the phase diagram which is much thinner for $B_{ss}(1) = 100$ and contains more holes than that for $B_{ss}(1) \approx 44.5$. This phase diagram is similar to that of Fig. 8 of Ref. [12].

As discussed previously for single-component annular liquid jets [12], the broadening of the power spectrum and the appearance of holes in the phase diagram are indicative of the presence of chaos. However, the transition from the periodic motion for $B_{ss}(1) = 25$ to the chaotic one corresponding to $B_{ss}(1) = 100$ does not seem to follow a standard scenario such as that of Ruelle-Takens at least for sufficiently large values of $B_{ss}(1)$; in fact, it has been observed that the transition to chaos for large values of $B_{ss}(1)$ is rather abrupt or explosive, whereas, for smaller values of $B_{ss}(1)$, it has been observed that $R(t, 1)$ evolves from a fixed point to a periodic motion and then to a quasiperiodic motion and chaos as $B_{ss}(1)$ is increased.

It is remarkable to notice that the results of the three time-dependent studies discussed in the previous paragraphs exhibit phase diagrams and power spectra similar to the ones observed in hollow, annular liquid jets [12] despite the differences in the geometry and boundary conditions, i.e. a single-component, hollow, annular jet is characterized by two free surfaces, whereas a bi-component or compound jet is characterized by a free surface, an inner–outer jet interface and symmetry conditions for the inner jet. This similarity indicates that the nonlinear dynamics of bi-component compound jets and single-component, annular jets are analogous for take-up velocities smaller and greater than that corresponding to the critical value determined in the linear stability analysis of the viscous flow regime. For this reason, no time-dependent results are shown in this paper, and only the effect of the flow parameters on $R(t, 1)$ are summarized in Table 1. This table shows that, for $Re = 1$, the compound jet behaves in a periodic manner with a frequency equal to that of the imposed velocity fluctuations, and there is very little difference between the largest and smallest values of $R(t, 1)$. The largest and smallest values of $R(t, 1)$ increase and decrease, respectively, as Re is decreased on account of the large gradients of the axial velocity at the downstream boundary which increase as Re is increased; a similar comment applies to the axial traction force at the take-up point. For the Reynolds number of the basic set of parameters of Table 1, the effects of the Froude number are small; however, the largest value of $R(t, 1)$ decreases as Re/F is increased on account of the increase in the gravitational pull as Re/F is increased.

Table 1 also shows that the effects of the capillary number are small, although a decrease in Ca results in an increase in the largest value of $R(t, 1)$. The effects of ρ_1/ρ_2, μ_1/μ_2 and σ_1/σ_2 on the nonlinear dynamics of compound liquid jets have been found to be small for the values of the parameters considered in Table 1. As should be expected, the largest value of $R(t, 1)$ increases as p_e is decreased.

5. Conclusions

The leading-order fluid dynamics equations of isothermal, axisymmetric, Newtonian, compound liquid jets at low Reynolds numbers have been derived by means of perturbation methods based on the slenderness ratio. It has been shown that these leading-order equations are one-dimensional and correspond to the conservation of mass and global linear momentum conservation, and are much simpler but depend on a larger set of parameters than those corresponding to single-component, annular jets, i.e. the Reynolds, Froude and capillary numbers, pressure of the surroundings, and density, viscosity and surface tension ratios.

Table 1

Maximum and minimum values of $R(t, 1)$ and axial traction forces on the inner and outer jets at the take-up point, and maximum spectral power and frequency associated with the maximum power of $R(t, 1)$: effects of the fluid dynamics parameters (phase diagram with holes, filled phase diagram and periodic behaviour are identified with superscripts 1, 2 and 3, respectively on the leftmost column; the basic set of parameters is $Re = 10^{-4}$, $Re/F = 0$, $Ca = 10^{39}$, $\rho_1/\rho_2 = 1$, $\mu_1/\mu_2 = 1$, $\sigma_1/\sigma_2 = 1$, $p_e = 0$, $Q_1 = 0.50$, $Q_2 = 1 - Q_1$, $B_{ss}(0) = 1$, Rad = 0.10, $B_{ss}(1) = 2Q_1/\mathrm{Rad}^2$; the upstream axial velocity is sinusoidally excited with an amplitude and frequency equal to 0.01 and 1, respectively)

Parameter	$R_{max}(t, 1)$	$R_{min}(t, 1)$	$F^{(1)}_{max}$	$F^{(1)}_{min}$	$F^{(2)}_{max}$	$F^{(2)}_{min}$	P	f
$Re = 0.1^2$	0.2737	0.0307	59.2482	1.5227	59.2482	1.5227	38.6010	2.1449
$Re = 1^3$	0.1009	0.0990	53.6308	51.6645	53.6308	51.6645	0.0092	0.16
$Re/F = 1^1$	0.4426	0.0161	56.8320	0.3583	56.8320	0.3583	38.5327	1.8849
$Re/F = 0.01^1$	0.4537	0.0154	59.1257	0.3354	59.1257	0.3354	31.7847	1.8299
$Ca = (10^5)^1$	0.4527	0.0155	58.8154	0.3386	58.8154	0.3386	37.7074	1.8299
$Ca = (10^2)^1$	0.4543	0.0154	59.0518	0.3359	59.0539	0.3360	32.6179	1.8249
$\rho_1/\rho_2 = 10^1$	0.4521	0.0156	58.9173	0.3418	58.9173	0.3418	28.9642	1.8299
$\rho_1/\rho_2 = 0.1^1$	0.4535	0.0155	58.6993	0.3371	58.6993	0.3371	38.7148	1.8299
$\mu_1/\mu_2 = 10^1$	0.4529	0.0155	590.8526	3.3816	59.0853	0.3382	38.7382	1.8299
$\mu_1/\mu_2 = 0.1^1$	0.4535	0.0154	5.9194	0.0336	59.1943	0.3364	37.7181	1.8299
$\sigma_1/\sigma_2 = 10^1$	0.4527	0.0155	58.8597	0.3386	58.8597	0.3386	38.0239	1.8299
$Q_1 = 0.75^2$	0.3775	0.0193	70.0343	0.7411	23.3448	0.2470	41.0396	3.0798
$Q_1 = 0.25^1$	0.5650	0.0121	38.4789	0.1076	115.4367	0.3227	31.2553	0.7950

Analytical solutions to the leading-order steady state equations have been obtained for four different flow regimes. For the steady viscous regime, a linear stability analysis is shown to be governed by the same eigenvalue equation as that for the spinning of isothermal, round jets and single-component, annular jets at zero Reynolds numbers.

Numerical results of the time-dependent leading-order equations indicate that, as the axial velocity at the downstream boundary is increased, the radius of the inner round jet at the take-up point evolves from a fixed point to a periodic motion to a broad spectrum. The phase diagrams of this radius may exhibit holes, i.e. regions which are not visited, when the axial velocity component at the take-up boundary is sufficiently large, thus indicating the presence of chaos. These phase diagrams are similar to the ones found for single-component annular liquid jets. It has also been shown that the compound jet's radii and axial traction force at the take-up point exhibit very sharp spikes whose separation depends on the Reynolds, Froude and capillary numbers, density, viscosity and surface tension ratios, and location, amplitude and frequency of the imposed velocity perturbations. These spikes are somewhat modulated with a lower frequency which is of the order of that of the imposed axial velocity perturbation.

Acknowledgements

The research reported in this paper was supported by Project PB97-1086 from the D.G.E.S. and Project BFM2001-1902 of the Dirección General de Investigación of Spain.

References

[1] Pearson JRA. Mechanics of polymer processing. New York: Elsevier, 1985.
[2] Pearson JRA, Matovich MA. Spinning a molten threadline. Ind Chem Engng Fund 1969;18:605–9.
[3] Schultz WW, Davis SH. One-dimensional liquid fibers. J Rheol 1982;26:331–45.
[4] Park C-W. Extensional flow of a two-phase fiber. AIChE J 1990;36:197–206.
[5] Lee W-S, Park C-W. Stability of a bicomponent fiber flow. ASME J Appl Mech 1995;62:511–6.
[6] Ji C-C, Yang J-C. Mechanics of steady flow in coextrusion fiber spinning. Polym Engng Sci 1996;36:1399–409.
[7] Ji C-C, Yang J-C, Lee W-S. Stability of Newtonian coextrusion fiber spinning. Polym Engng Sci 1996;36:2685–93.
[8] Naboulsi SK, Bechtel SE. Bicomponent Newtonian fibers. Phys Fluids 1999;11:807–20.
[9] Ramos JI. Asymptotic analysis of compound liquid jets at low Reynolds numbers. Appl Math Comput 1999;100:223–40.
[10] Schultz WW. Slender viscoelastic fiber flow. J Rheol 1987;31:733–50.
[11] Schultz WW, Davis SH. Effects of boundary conditions on the stability of slender viscous fibers. ASME J Appl Mech 1984;51:1–5.
[12] Ramos JI. Drawing of annular liquid jets at low Reynolds numbers. Comput Theor Polym Sci 2001;11:429–43.